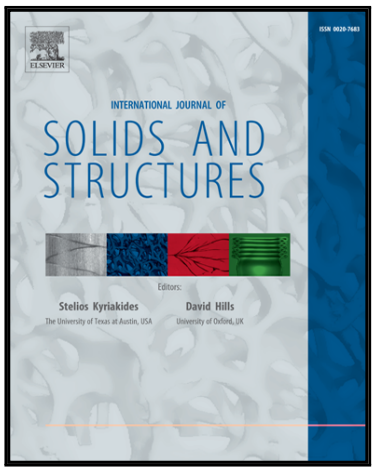

Damage Prediction in Single Point Incremental Forming using an Extended Gurson Model

Carlos Felipe Guzmán, Sibo Yuan, Laurent Duchêne,
Erick I. Saavedra Flores, Anne Marie Habraken

PII: S0020-7683(17)30164-6
DOI: 10.1016/j.ijsolstr.2017.04.013
Reference: SAS 9536

To appear in: *International Journal of Solids and Structures*

Received date: 29 November 2016
Revised date: 17 March 2017
Accepted date: 12 April 2017

Please cite this article as: Carlos Felipe Guzmán, Sibo Yuan, Laurent Duchêne, Erick I. Saavedra Flores, Anne Marie Habraken, Damage Prediction in Single Point Incremental Forming using an Extended Gurson Model, *International Journal of Solids and Structures* (2017), doi: 10.1016/j.ijsolstr.2017.04.013

Damage Prediction in Single Point Incremental Forming using an Extended Gurson Model

Carlos Felipe Guzmán[a], Sibo Yuan[b], Laurent Duchêne[b], Erick I. Saavedra Flores[a,*], Anne Marie Habraken[b,c]

[a] *Departamento de Ingeniería en Obras Civiles, Universidad de Santiago de Chile, Av. Ecuador 3659, Estación Central, Santiago, Chile*
[b] *Université de Liège, Department ArGEnCo, Quartier Polytech 1, Allée de la découverte 9, 4000, Liège, Belgium*
[c] *Research Director of the Fonds de la Recherche Scientifique - FNRS, Belgium*

Abstract

Single point incremental forming (SPIF) has several advantages over traditional forming, such as the high formability attainable by the material. Different hypotheses have been proposed to explain this behavior, but there is still no straightforward relation between the particular stress and strain state induced by SPIF and the material degradation leading to localization and fracture. A systematic review of the state of the art about formability and damage in SPIF is presented and an extended Gurson-Tvergaard-Needleman (GTN) model was applied to predict damage in SPIF through finite element (FE) simulations. The line test was used to validate the simulations by comparing force and shape predictions with experimental results. To analyze the failure prediction, several simulations of SPIF cones at different wall angles were performed. It is concluded that the GTN model underestimates the fail-

*Corresponding Author
Email addresses: cf.guzman@usach.cl (Carlos Felipe Guzmán), s.yuan@ulg.ac.be (Sibo Yuan), l.duchene@ulg.ac.be (Laurent Duchêne), erick.saavedra@usach.cl (Erick I. Saavedra Flores), anne.habraken@ulg.ac.be (Anne Marie Habraken)

ure angle on SPIF due to wrong coalescence modeling. A physically-based Thomason coalescence criterion was then used leading to an improvement on the results by delaying the onset of coalescence.

Keywords: Single Point Incremental Forming, Ductile fracture, Gurson model, Finite Element Method

2010 MSC: 74R99, 74S05

1. Introduction

Nowadays, product manufacturing can be divided into two groups: relatively simple products manufactured in a mass production chain and specialized components produced in reduced batches. Within the second group, prototyping through incremental sheet forming (ISF) has been the subject of several studies during the last decade (Jeswiet et al., 2005; Reddy et al., 2015). ISF refers to processes where the plastic deformation occurs by repeated contact between a relatively small tool and a clamped sheet metal. The small zone submitted to plastic deformation moves during the whole process, covering the whole product and giving the final shape.

The focus of this work is the single point incremental forming (SPIF) process variant, where the sheet metal is deformed by a single spherical tool, which follows a complex path in order to get the required shape. One of the most prominent characteristics of the SPIF process is its flexibility. Since the shape is only given by the motion of the tool, no die is needed. The toolpath can easily be controlled using a CAD software and a change of the final shape can be quickly and inexpensively made. This dieless nature makes the SPIF process to be appropriate for prototyping, highly personalized pieces

and other shell-like structures. Conversely, and depending on the tool path length, the forming process can reach hours. It is, by consequence, adapted to small batch production and rapid prototyping. Applications range from large pieces like car fenders or plastic moulds, to small parts such as medical implants or prostheses.

Another interesting feature of the SPIF process is the deformation attainable by the sheet before fracture. SPIF can reach very large levels of deformation, even larger than conventional processes like the hemispherical dome (punch) test (Filice et al., 2002) or deep drawing (Jeswiet et al., 2005). The explanation of this behavior has been deeply investigated but a wide spectrum of questions still remain unanswered (Reddy et al., 2015).

In the present research, finite element (FE) simulations were used to predict damage and fracture in the SPIF process. The article is organized as follows. Section 2 presents a literature review about damage investigations on SPIF, including some notes about the traditional formability analysis. Section 3 describes the constitutive model and the material parameters used to simulate the sheet metal. Section 4 outlines the SPIF tests used to investigate damage and failure. The FE simulations and their results are also discussed here in detail. The article ends with the conclusions presented in section 6.

In terms of notation, the vectors and second order tensors are denoted by boldface letters, while the scalars are plain letters. $\mathbb{H}$ represents a fourth order tensor.

2. State of the art

SPIF and its variants have been covered by several authors. One of the first review articles of the process was written by Jeswiet et al. (2005), covering from the experimental setup to FE analysis. Emmens and van den Boogaard (2010) published a review of technical developments on incremental forming through the years. It is important to note that the review from Emmens and van den Boogaard (2010) is more focused on ISF than SPIF. Recently, Reddy et al. (2015) reviewed SPIF concentrating their efforts in the shape accuracy and formability.

In this work the focus is on formability and damage leading to fracture. Formability can be understood as the ability of a material to undergo a certain amount of plastic deformation without significant damage and/or fracture. Damage prediction is linked to the formability and the deformation mechanisms, as it will be seen in the following sections.

2.1. Formability

As mentioned in the introduction, SPIF is characterized by an exceptionally large formality when compared to other forming processes. These observations have prompted the characterization and study of the SPIF forming limits for different materials and geometries. The approach towards the understanding of the increased formability can be divided in three categories: the application of formability characterization methodologies, like forming limit diagrams (FLD), the study of the effect of particular SPIF process parameters on the material formability, and the prediction of rupture by FE modeling.

Most of the formability studies about sheet metal are rigorously embodied using a FLD concept, to detect a (diffuse or localized) necking condition followed by a rupture phase. FLDs were initially introduced by Keeler and Backofen (1963) and Marciniak and Kuczynski (1967). This commonly used framework has been widely adopted in the literature but suffers from important drawbacks when applied to SPIF (Emmens and van den Boogaard, 2009). Non radial strain paths, high stress gradients along the sheet thickness and the presence of through-thickness shear implying that the principal strains are not in the sheet plane are characteristics of SPIF. These specificities do not respect the assumption of FLD and their use can lead to wrong conclusions (Allwood et al., 2007; Emmens and a.H. van den Boogaard, 2007). Hence, FLDs should be regarded only as an useful tool providing important insights on the material formability but not as the definitive tool to characterize it.

A short review of the mechanisms claimed to enhance SPIF formability were listed by Emmens and van den Boogaard (2009) and further detailed in Emmens (2011). An overview of some of them is given hereafter:

Through-thickness shear. In theory, under simple shear, necking is not developed and rupture appears by shear band. In stretch forming, shear brings a stabilization effect by reducing the yield stress in tension, as shown by Emmens and van den Boogaard (2009). Shear can explain the increase of the SPIF formability, as analytically shown by Allwood et al. (2007) and Eyckens et al. (2009), using an extended Marciniak and Kuczynski (1967) model.

Bending-under-tension (BUT). Also referred to as stretch bending, BUT is another stress state presenting an improved formability (Emmens and

van den Boogaard, 2008). It shows a considerable increase in formability when compared to cases without bending. Neglecting the stabilizing effect of bending, the conventional FLD, which assumes homogeneous stress along the thickness direction, may underestimate the forming potential. One way to overcome this drawback is to formulate the FLD in the principal stress space, instead of using (the traditional) strain-based FLD (Stoughton and Yoon, 2011).

Cyclic effects. It must be noted that during SPIF the strain history is not proportional because of successive bending and unbending around the tool. Cyclic loading, generated by serrated strain paths, has been widely observed in FE simulations within the ISF literature (Flores et al., 2007; Eyckens et al., 2007; Seong et al., 2014) but also experimentally through digital image correlation (DIC) measurements (Eyckens et al., 2010). This cyclic effect can have a great influence on formability, as demonstrated by Eyckens et al. (2007).

In a SPIF hardware setup, several parameters were changed to identify the key parameters. The wall angle and sheet thickness seem to be the most relevant parameters in terms of formability. For a chosen material, the tool diameter and step-down size play a minor role on the forming angle (Ham and Jeswiet, 2007). As mentioned by Behera (2013), SPIF is characterized by well defined forming limits for a specific material thickness and process parameters. Hence, the maximum draw angle of SPIF cones can be used as a formability indicator. It is useful to note that failure does not take place immediately in a part with a wall angle above the failure limit; it

occurs at a certain depth. The stress state within a cone formed by SPIF can be linked to the *sine law* (Jeswiet et al., 2005), and it is possible for this geometry to establish a limit for thinning based on the wall angle and the initial thickness. Thus, it is straightforward to hypothesize that in order to increase the maximum wall angle, one could increase the initial thickness. However, this strategy has its practical limitations like the maximum machine load and thickness specifications of the material batch (Duflou et al., 2008).

2.2. Damage and fracture prediction

Formability analysis by FLD has been for long time the traditional way to optimize the sheet metal forming operations. However, damage modeling offers another methodology based on the mechanisms of degradation/softening leading to final fracture. Of course, formability and damage prediction can easily be linked, however they are essentially different. Formability can be regarded as a more practical (engineering) concept. Material and process parameters generate a post-processed strain history using FLDs, while the material damage is an approach based on a particular stress or strain field histories acting in a material continuum. Damage is characterized in continuum mechanical models by a specific damage variable evolving until a limit is reached at the onset of crack formation (Lemaitre, 1985; Chow and Wang, 1987; Voyiadjis and Kattan, 1992; Brünig, 2003). Another fundamental difference between these approaches is that during damage development, the microscopic scale is not negligible, so the analysis should permanently be regarded as material dependent and needs to model the microstructure evolution (Garrison and Moody, 1987). The literature review shows a relatively scarce amount of SPIF research related to damage. One possible explanation

is that damage analysis does not often provide simplified solutions in terms of the forming process parameters. Moreover, complex damage models require complex characterization methodologies, which are not always feasible.

Porosity-induced damage within SPIF process has been studied, for instance, by Lievers et al. (2004) and Hirt et al. (2004). Lievers et al. (2004) presented a novel method to identify void nucleation parameters of a Gurson model using SPIF. This approach is sustained under the hypothesis that in some forming processes, like stretching, stretch flanging and SPIF, necking is suppressed and formability is controlled by void damage and shear band instability. Quadrangular SPIF pyramids for different aluminum alloys and wall angles were formed by Lievers et al. (2004), allowing an easy measurement of porosity.

Hirt et al. (2004) performed a simulation of a truncated pyramid formed using multi-stage forming, using a partial die. To study the stress state, the Gurson-Tvergaard-Needleman (GTN) model was used together with shell elements. Despite the limitations of the shell elements, the predictions showed that higher forming limits can be achieved with small forming heads and large values for the vertical pitch.

Silva et al. (2008) provided a theoretical model for a rotational symmetric SPIF shape, based on a membrane analysis. Sheet stretching was considered but bending and shear were neglected. It was observed that the opening mode of cracks in SPIF is similar to the one present in conventional stamping (mode I in fracture mechanics). The characterization of the stress state within the wall is given assuming plane strain condition (Filice et al., 2002; Jeswiet et al., 2005; Jeswiet and Young, 2005). In terms of damage evolution, the

decrease of the sheet thickness (or increase of the tool radius) shifts the Mohr circle to the tensile region, thus increasing the hydrostatic stress and the accumulated damage. This result is consistent with the findings of Hirt et al. (2004). The higher formability of SPIF process, compared to conventional stamping, is explained in terms of the meridional stress. In stamping, the level of hydrostatic stress in biaxial stretching is higher than in plane strain (and in the SPIF process), so damage grows faster.

Silva et al. (2011) grouped the literature review in two families: the *necking view*, where formability is limited by necking and the raise of formability is due to stabilization mechanisms of the necking; and the *fracture view*, where formability is limited by fracture. High levels of formability come as a result of suppression of necking or low damage growth. Each view has its advantages and drawbacks. Against the necking view, it is known that forming limits in SPIF are well above conventional FLD and closer to the fracture forming limits (FFL). On the other hand, the fracture approach requires that all possible strains located on a specific limit to be dependent only on the material properties. Nevertheless, it is shown that the FFL can be sensitive to the tool size. Experimental studies show that the onset of the crack seem to be dependent on the formed shape. Silva et al. (2011) proposed a threshold where, depending on the tool radius, there is a transition between SPIF and stamping. Then crack prediction is expressed in terms of necking/suppression of necking. However, this view is not clear because localization can be a characteristic of SPIF.

Malhotra et al. (2012) used the Xue (2007) damage model to predict the mechanics of fracture on a SPIF cone and funnel through FE simulations.

The Xue (2007) model is a coupled damage model which combines plastic strain, hydrostatic pressure and shear on fracture. One of the main features of this model is that not only damage accumulation and fracture can be predicted, but also the occurrence of diffused and localized necking (Xue and Belytschko, 2010). It is observed in the funnel shape that the initial damage is low due to the low initial angle and it increases dramatically until reaching an angle higher than 70°. It is also noticed that the shear strain is higher in the element from the inner side (i.e. the side making contact with the tool) of the sheet, delaying damage accumulation. Nevertheless, the Xue (2007) model predicts faster damage accumulation in SPIF than in deep drawing (in which the shear is small and the deformation mechanism is governed by stretching). However, failure in SPIF is greatly delayed and the sheet can achieve a larger deformation without failure than in deep drawing. Two observations can be regarded at this point. One is that from the observed thinning, plastic deformation is evenly distributed so the first localization has still to undergone neck growth when the direct tool force is already far. This fact justifies the ability of the shear band to *share* some subsequent deformation. The second observation is that if a section is still undergoing deformation after localization, it should break in this point instead of in the contact zone (as it is observed experimentally). Malhotra et al. (2012) suggested that since the distance from the neck to the load application increases, the ability of this neck to share deformation decreases.

Here, the localized effect of SPIF implies that the plastic strain is distributed more evenly in the piece than in deep drawing. The already formed zone is still undergoing plastic deformation. This can explain the inability of

conventional FLD to predict failure in SPIF, and justifies the observed slow transition between material localization and actual fracture.

Summarizing, the classical way to analyze the high formability within FLD can help to understand the effect of the process parameters. For instance, the results obtained by FLDs suggest that through-thickness shear (TTS) is an important stabilization mechanism. However, the complexity of SPIF seems to go beyond the scope of the FLD approach. Malhotra et al. (2012) showed that TTS by itself cannot explain the high formability. Comparing with the formability review of Section 2.1, the localized effect of BUT seems to be more important than TTS. Moreover, Silva et al. (2011) showed that the part geometry and the tool size can have a coupled effect on the formability. The effects of the thickness distribution prior to necking or failure without necking are hard to capture by a classical formability analysis. Damage models, on the other hand, allow a more comprehensive understanding of the material behavior leading to fracture. It is not hard to observe that both approaches can be complementary. Experimental results from the FLD can be used to validate damage models.

3. Constitutive model

In this section, the constitutive models for the plastic and damage behavior of the material is briefly explained. The elastic part is described by the isotropic-linear version of the Hooke's law.

3.1. Elasto-plastic behavior

The Hill (1948) yield criterion is chosen because of its overall simplicity when describing the anisotropic behavior of a metallic material. The shape

of this yield locus is given by the following equation:

$$\sigma_{eq} := \sqrt{\frac{1}{2}(\boldsymbol{\sigma} - \boldsymbol{X}) : \mathbb{H} : (\boldsymbol{\sigma} - \boldsymbol{X})}, \tag{1}$$

where $\mathbb{H}$ is a fourth-order tensor containing the anisotropic parameters and σ_{eq} is the equivalent stress. Within the anisotropic axis frame (and omitting the backstress for the sake of simplicity), the shape of the yield locus can be written as:

$$\begin{aligned} 2\sigma_{eq}^2 := F(\sigma_y - \sigma_z)^2 + G(\sigma_z - \sigma_x)^2 + H(\sigma_x - \sigma_y)^2 + \dots \\ \dots + 2L\sigma_{yz}^2 + 2M\sigma_{zx}^2 + 2N\sigma_{xy}^2, \end{aligned} \tag{2}$$

where F, G, H, L, M and N are material parameters.

Assuming a *strain hardening* hypothesis, the isotropic hardening behavior can be modeled by the Swift law which shows neither saturation nor softening phenomenon:

$$\sigma_Y\left(\bar{\epsilon}^P\right) = K\left(\bar{\epsilon}^P + \epsilon_0\right)^n, \tag{3}$$

where σ_Y is the yield stress, $\bar{\epsilon}^P$ the equivalent plastic strain and ϵ_0, K, n are material parameters. An evolution law for the backstress tensor was proposed by Armstrong and Frederick (1966) (A-F model), including a non-linear term (Chaboche, 1977; Frederick and Armstrong, 2007):

$$\dot{\boldsymbol{X}} = C_X\left(X_{\text{sat}}\dot{\boldsymbol{\epsilon}}^P - \boldsymbol{X}\bar{\epsilon}^P\right), \tag{4}$$

where $\dot{\boldsymbol{X}}$ is the rate of the *backstress* tensor, $\dot{\boldsymbol{\epsilon}}^P$ is the plastic strain rate tensor. C_X (saturation rate) and X_{sat} (saturation value of the backstress) are material constants. The model is able to predict both the Bauschinger effect and accumulation of plastic strain under an asymmetrical stress cycle.

3.2. Damage model

The Gurson (1977) model is a mathematical representation of ductile damage based on the micromechanics of the material. It is defined by an homogenization theory in the analysis of the plastic stress field in a microscopic medium composed of a dense matrix and cavities. The model is expressed as a macroscopic yield criterion, introducing a micromechanical variable as its damage parameter: the *void volume fraction* f, which acts as an imperfection during the plastic flow.

The Gurson-Tvergaard-Needleman (GTN) model is one of the first extensions to robustly compile the three stages of damage development: void nucleation, growth and coalescence. The evolution of voids can be mathematically assumed to be additively decomposed in a nucleation and growth part:

$$\dot{f} = \dot{f}_n + \dot{f}_g, \tag{5}$$

where f_n is the nucleated void volume fraction and f_g the growth of the voids, derived from the plastic incompressibility of the matrix:

$$\dot{f}_g = (1 - f)\, tr\dot{\boldsymbol{\epsilon}}^p. \tag{6}$$

Nucleation can be correlated in terms of the equivalent plastic strain in the matrix ϵ_M^P in the following form (Chu and Needleman, 1980):

$$\dot{f}_n = \frac{f_N}{S_N\sqrt{2\pi}} \exp\left[-\frac{1}{2}\left(\frac{\epsilon_M^P - \epsilon_N}{S_N}\right)^2\right], \tag{7}$$

where f_N is the maximum potential nucleated void volume fraction in relation with the inclusion volume fraction, ϵ_N is the mean effective plastic strain of

the matrix at incipient nucleation and S_N is the Gaussian standard deviation of the normal distribution of inclusions.

The third stage, coalescence, is characterized at the macroscopic level in a load-displacement curve by an abrupt change in the slope at the onset of a (macroscopic) crack. In order to incorporate coalescence into the Gurson model, Tvergaard and Needleman (1984) proposed to identify the porosity evolution as an addition of nucleation and growth porosity rates and by a specific coalescence function f^*, which replaces the porosity in the following way:

$$f^* = \begin{cases} f & \text{if } f < f_{cr} \\ f_{cr} + K_f(f - f_{cr}) & \text{if } f > f_{cr} \end{cases} \tag{8}$$

with

$$K_f = \frac{f_u - f_{cr}}{f_F - f_{cr}}, \tag{9}$$

where f_u is the ultimate value of f^* at the occurrence of ductile rupture, f_{cr} is the critical void volume fraction at the onset of coalescence and f_F is the porosity at final failure. The aim of f^* is to model the complete vanishing of the carrying load capacity due to void coalescence.

The yield criterion of the GTN model introduces the factors q_1 and q_2 to describe more accurately void growth mechanics (Tvergaard, 1981):

$$F_p(\boldsymbol{\sigma}, f, \sigma_Y) = \frac{\sigma_{eq}^2}{\sigma_Y^2} - 1 + 2q_1 f \cosh\left(-\frac{3q_2}{2}\frac{\sigma_m}{\sigma_Y}\right) - (q_1 f)^2 = 0, \tag{10}$$

where σ_m is the mean (hydrostatic) stress. Using a value of q_1 =1.5 and q_2 =1.0 allows the continuum model to be in good agreement with the localization strain (Tvergaard, 1981).

3.2.1. Thomason criterion

The coalescence model in the GTN model is a purely phenomenological approach, but physically-based coalescence criteria can also be used. For instance, Zhang et al. (2000) incorporated a criterion based on the plastic limit load proposed by Thomason (1990). This model has good accuracy for both hardening and non-hardening materials. As mentioned previously, coalescence in the GTN model is triggered when the porosity reaches a critical value f_{cr} and the evolution of voids is accelerated through the effective porosity f^* function. The critical coalescence porosity f_{cr} is a material parameter in the classical GTN model. In the Thomason criterion, on the contrary, this threshold is supposed to be reached when the following inequality is no longer satisfied:

$$\frac{\sigma_I}{\sigma_Y} < \left[\alpha\left(\frac{1}{\chi}-1\right)^2 + \frac{\beta}{\sqrt{\chi}}\right]\left(1-\pi\chi^2\right), \tag{11}$$

where σ_I is the maximum principal stress, α is a material parameter defined as a function of the hardening exponent n and β =1.24. The void space ratio χ is given by:

$$\chi = \frac{2\sqrt[3]{\frac{3f}{4\pi}\exp\left(\epsilon_1+\epsilon_2+\epsilon_3\right)}}{\sqrt{\exp\left(\epsilon_1+\epsilon_2+\epsilon_3-\epsilon_{\max}\right)}}, \tag{12}$$

with ϵ_1, ϵ_2 and ϵ_3 the principal strains, and $\epsilon_{\max}$ the maximum principal strain.

3.2.2. Shear extension

The Gurson (1977) model and the GTN extension include the triaxiality and the mean (hydrostatic) stress as scalar parameters describing the stress state. Nevertheless, Gologanu et al. (1996) observed that the void expansion

can vary in different directions under the same triaxiality. Furthermore, the Gurson model does not behave very well under low values of triaxiality (< 0.3). In some cases like in shear-dominated deformations, triaxiality is near zero or even negative predicting almost no increase of damage (in the GTN extension of the Gurson model voids do not grow under pure shear).

The effect of the stress invariants on the mechanical behavior is not limited only to the use of the triaxiality or the mean stress. The third invariant (related to the Lode angle) of the deviatoric stress has been considered in constitutive models to predict localization (Brünig et al., 2000) and fracture (Bai and Wierzbicki, 2008). Barsoum and Faleskog (2007) showed that the strain localization decreases when passing from tension to shear, and the softening rates decreases when increasing the Lode parameter. Gao et al. (2009) demonstrated that the Lode parameter has an important effect on the strain at coalescence and this effect is lower at high triaxiality, coinciding with the previous results from Zhang et al. (2001).

Encouraged by this evidence, Nahshon and Hutchinson (2008) proposed a shear extension for the Gurson model involving the void growth relation (Eq. 5). Hence, the void rate is now governed by three terms:

$$\dot{f} = \dot{f}_n + \dot{f}_g + \dot{f}_s, \tag{13}$$

where f_s is the contribution by the shear damage. The influence of the Lode angle is then given by:

$$\dot{f}_s = k_\omega f \omega(\boldsymbol{\sigma}) \frac{\boldsymbol{\sigma}_{\text{dev}} : \dot{\boldsymbol{\epsilon}}^P}{\sigma_{eq}}, \tag{14}$$

with $\boldsymbol{\sigma}_{\text{dev}}$ the deviatoric part of the Cauchy stress tensor, k_ω a material

constant and $\omega(\boldsymbol{\sigma})$ a stress scalar function defined as:

$$\omega(\boldsymbol{\sigma}) = 1 - \left(\frac{27}{2}\frac{J_3}{\sigma_{eq}^3}\right)^2; \qquad 0 \leq \omega \leq 1, \tag{15}$$

where J_3 is the third deviatoric stress invariant. This extension has however a less straightforward link with the microstructure. f_s is more related to the void shape and void rotation, and their impact on the stress field distribution within the matrix. Like the coalescence extension, shear extensions are purely phenomenological and thus the *void porosity* loses its original meaning for a more general damage representation.

In Nielsen and Tvergaard (2009, 2010) it has been noted the strong contribution of f_s in plane strain uni-axial tension, even if the triaxiality T is high. A triaxiality T dependent weight function $\Omega(T)$ is proposed. In Eq. 14, $\omega(\boldsymbol{\sigma})$ is replaced by ω_0 defined as:

$$\omega_0 := \omega(\boldsymbol{\sigma})\Omega(T), \tag{16}$$

where $\Omega(T)$ is a function which linearly decreases depending on the triaxiality:

$$\Omega(T) = \begin{cases} 1 & \text{if } T < T_1 \\ (T - T_2)/(T_1 - T_2) & \text{if } T_1 \leq T \leq T_2 \\ 0 & \text{if } T > T_2 \end{cases}, \tag{17}$$

where T_1 and T_2 are material parameters.

3.2.3. Anisotropic plasticity and mixed hardening of the matrix

The original Gurson model is based on a development where the matrix surrounding the void is perfectly plastic and obeying to the von Mises yield criterion. Benzerga and Besson (2001) incorporated anisotropy into the

Gurson (1977) model and the GTN model based on experimental evidence regarding the effect of matrix flow on particle debonding (and hence in void evolution). This new yield criterion is defined by:

$$F_p(\boldsymbol{\sigma}, f, \sigma_Y) = \frac{\sigma_{eq}^2}{\sigma_Y^2} - 1 + 2q_1 f \cosh\left(-\frac{3q_2}{\kappa}\frac{\sigma_m}{\sigma_Y}\right) - (q_1 f)^2 = 0, \quad (18)$$

which is the same as Eq. 10 but incorporates the effect of the anisotropy through σ_{eq} and the coefficient κ.

In order to introduce isotropic hardening in the matrix, an heuristic approach is followed using the Swift law (defined previously in Eq. 3). For the kinematic hardening, classical evolution equations like the A-F model (Eq. 4) have been used previously within the Gurson model family (Mühlich and Brocks, 2003; Ben Bettaieb et al., 2011).

3.3. Material parameters identification

The selected material for the experimental campaign is a DC01 steel sheet of 1.0 mm thickness. The plastic behavior, including anisotropy and hardening, is characterized by an experimental testing campaign involving homogeneous stress and strain fields (tensile tests in three directions, notch tensile tests, cyclic and static shear test, microscopic investigations, etc.). Details about the experimental tests, the identification methodology, the validation of the identified parameters, as well as the model choice are available in Guzmán (2016).

The material exhibits large ductility, being able to reach large displacement before fracture and an anisotropic behavior at 45° of the RD. The anisotropic coefficients of the Hill (1948) were identified using tensile tests

in three orthogonal directions plus a simple shear test. The set of plastic parameters is given in Table 1.

Table 1: Plasticity parameters identified for the SPIF simulations.

Anisotropy coefficients	Isotropic hardening	Kinematic hardening
F =0.81	K =542.49 MPa	C_X =113.63
G =0.99	ϵ_0 =1.78×10^{-2}	X_{sat} =81.96 MPa
H =1.46	n =0.4328	
N =2.92		

The GTN model includes several parameters of different nature. Some of them have micromechanical roots while others are strictly phenomenological. Hence, a methodology has been developed in order to obtain a robust set of parameters with both numerical and physical meanings. The methodology involves a macroscopic testing campaign with notched specimens and microscopic measurements of the void volume fraction. The model parameters are fitted to match the experimental results of force and strain field distribution identified by DIC.

Taken the plasticity parameters from Table 1 (hereafter called `Swift+AF` set) as the reference plastic parameters, Table 2 presents the model parameters obtained for different extensions of the anisotropic GTN model limited to void growth. `nuc` means that the void nucleation term f_n is added, `coa` that the latter model is improved by the function f^* of void coalescence and `shear` extends the `coa` model with the f_s term of shear damage, as defined by Eq. 13-17. For further details on the plastic and damage parameter identification, refer to Guzmán (2016).

Table 2: GTN model parameters identified for the SPIF simulations.

		Nucleation			Coalescence		Shear
Set name	f_0	f_N	S_N	ϵ_N	f_c	f_F	k_ω
`nuc`	0.0008	0.0025	0.175	0.42	-	-	-
`coa`	0.0008	0.0025	0.175	0.42	0.0055	0.135	-
`shear`	0.0008	0.0025	0.175	0.42	0.0055	0.135	0.25

4. SPIF simulations

In all subsequent simulations, the non-linear finite element code LAGAMINE is used. It is a lagrangian code developed by the ArGEnCo department of the University of Liège (Cescotto and Grober, 1985). The extended GTN model is implemented in the FE code using an implicit integration scheme (Ben Bettaieb et al., 2011; Guzmán and Saavedra Flores, 2016).

Due to the important stress and strain gradients found in the sheet during SPIF and the use of a 3D material model, the Reduced Enhanced Solid Shell (`RESS`) element (Alves de Sousa et al., 2005, 2006; Ben Bettaieb et al., 2015) is used because of its good balance between accuracy and CPU time. This element is based on the *solid-shell* element concept, which basically lies between a four-noded shell element and a eight-noded solid element. Hence, it is possible to model very thin (large aspect ratio) structures using 3D element models (like eight-noded brick elements) without any type of 2D hypothesis (like four-noded shell elements).

In order to avoid locking issues, numerical techniques such as the *enhanced assumed strain* (EAS) technique (Simo and Rifai, 1990), stabilization for the

reduced integration (Li and Cescotto, 1997) and the B-bar method (Alves de Sousa et al., 2005) are implemented at the element level.

Contact between the tool and the sheet is modeled using the `CFI3D` element, which is based in the penalty approach and Coulomb's friction law (Cescotto and Charlier, 1993; Habraken and Cescotto, 1998).

4.1. Line test

The line test is one of the simplest form of SPIF. It is accurately described by Bouffioux et al. (2011). The large size of the step-down (5 mm) induces larger stress gradients than in classical SPIF problems. It allows verifying the accuracy of the identified set of material parameters and to study SPIF deformation mechanisms. The stress and strain histories during the test are similar to the ones found in SPIF test of a simple geometry. In this research, a squared sheet of 182 mm $\times$ 182 mm and 1 mm thickness of DC01 steel is clamped along its edges, as shown in Fig. 1(a). A non-rotating spindle tool of diameter 10 mm is used, following a certain toolpath (Fig. 1(b)). The test was experimentally performed at KULeuven. In order to ensure the reproducibility of the results, the whole line test was performed three times and the bolts of the frame were tightened using the same torque.

4.1.1. FE simulation

The FE mesh is depicted in Fig. 1(c). It consists in 806 `RESS` solid-shell elements, one element layer with 3 integration points through-thickness and 806 `CFI3D` elements with 4 integration points. Symmetric boundary conditions are used along the X axis (Y =0) so only half of the sheet is simulated. The tool force is computed by a static implicit strategy. No

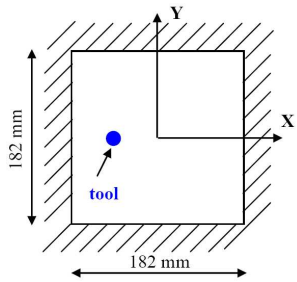

(a) Top view of the squared sheet showing the clamped edges.

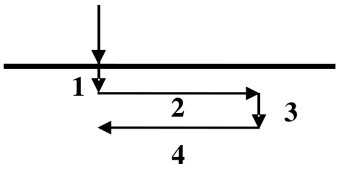

(b) Tool displacement.

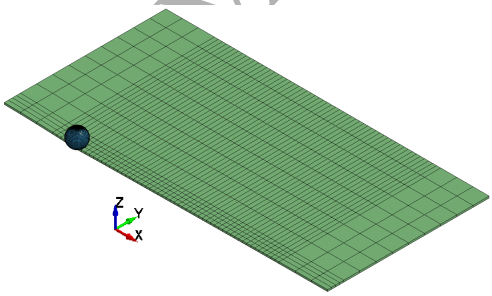

(c) FE mesh and tool tip.

Figure 1: Geometry and mesh of the line test.

friction is applied between the tool and the sheet.

4.1.2. Shape and force predictions

An experimental-numerical comparison of four different sets of material parameters is given in Fig. 2. The scale of the Z axis is not equal to the X axis in Fig. 2(a) in order to enhance the shape analysis, where the predicted curves are defined by the position of the nodes located in the top and bottom layers of the `RESS` element. The experimental results of the shape are obtained through a laser line scanner mounted on the machine. Fig. 2(a) shows the FE numerical results for a set of material parameters without damage (`Swift+AF`) and sets considering damage (`nuc`, `coa` and `shear`). Globally,

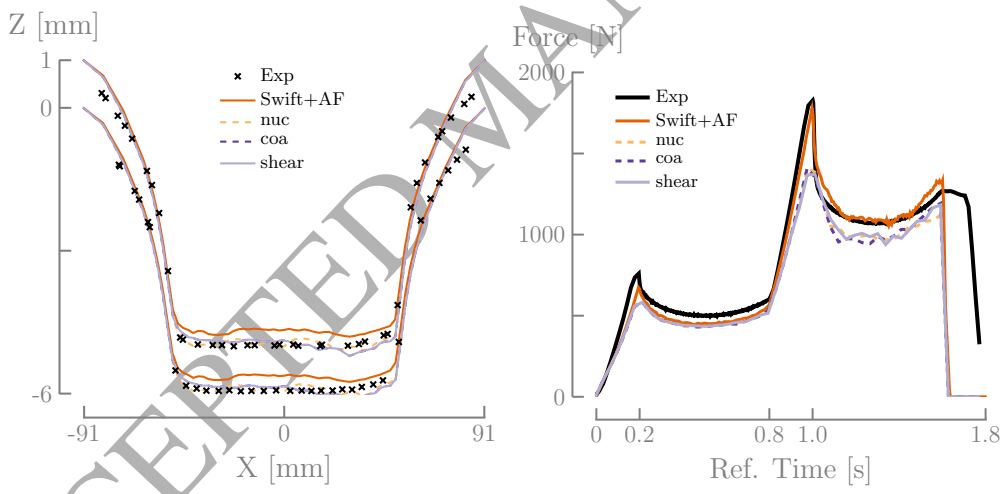

(a) Final shape. The predicted curves are defined by the position of the nodes located in the top and bottom layers of the FE mesh.

(b) Axial force evolution.

Figure 2: Shape and force prediction for the line test and comparison with experimental results.

the predicted shapes are in good agreement with the experimental results. The predictions using the GTN model are better than those using only plastic parameters. Nevertheless, the differences between the predicted shape by Hill (1948) or by the GTN model and the experimental measurements are less than 0.3 mm near X =0 mm, which is small compared to the shape depth (6 mm). The difference between sets considering damage or not is due to the softening effect induced by damage. In the simulations using the GTN model, no noticeable difference is observed among `nuc`, `coa` and `shear` sets.

Fig. 2(b) shows the tool reaction in the Z (axial) direction during the line test. The experimental force is measured using a load cell mounted on the machine. The predictions based on the set of parameters of the damage model (`nuc`, `coa` and `shear`) are slightly lower (less than 10%) than the ones associated with the plastic model (`Swift+AF`) using mixed hardening. Again, there is no important difference among the force predictions of damage activating nucleation and coalescence steps or taking into account a shear extension.

4.1.3. Analysis of state variables

The computed material state variables are analyzed within the simulations using the most complete GTN model (the `shear` set). The variables are retrieved from three different solid-shell elements: 118, 404 and 690, shown in Fig. 3. Element numbers 118 and 690 are located under the tool at the first (step 1 in Fig. 1(b)) and second indent (step 3), respectively. Element number 404 is located between these two elements. The results are shown in Fig. 4, where the indent step is depicted as a shaded area. The first integration point (closer to the outer surface, the one not making contact with the

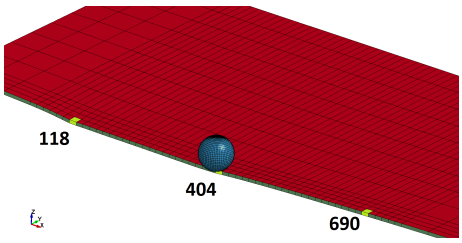

Figure 3: Line test FE mesh showing the number of elements (118, 404 and 690) selected to display state variables evolution.

tool) is found to give the highest equivalent plastic strain of the three integration points. This is expected, as the local stretching and bending of the sheet around the tool causes the zone in the outer side of the sheet to stretch more than zones in the inner side. Therefore, the state variables are analyzed at this integration point. From Fig. 4(a) showing the effective porosity f^* evolution, it is clear that the indent steps play a major role in the porosity history for the elements under the tool indentation (118 and 690). Element number 404 is not affected by the tool indentation as it is too far from the indentation zone. Nevertheless, there is a porosity increment due to the tool contact and sheet deformation. The porosity increment after each indent can be related with a triaxiality *peak* (marked with an arrow in Fig. 4(b)), when the tool approaches to the element. It can be observed that triaxiality increases when the tool approaches to the element, and decreases when the tool moves away from the (plastically deformed) element. It must be noted that even if the triaxiality is high for element numbers 404 and 690 during the first indent, there is no increment of the porosity as these elements do not deform plastically (see Fig. 4(c)) at this stage.

Triaxiality can explain why there is a porosity increment, but does not ex-

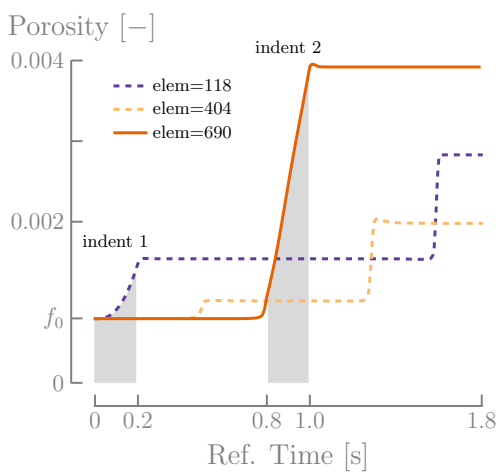

(a) Effective porosity.

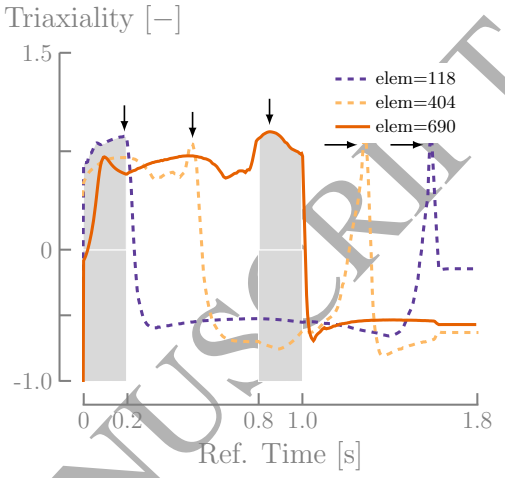

(b) Triaxiality. The arrows mark triaxiality *peaks*.

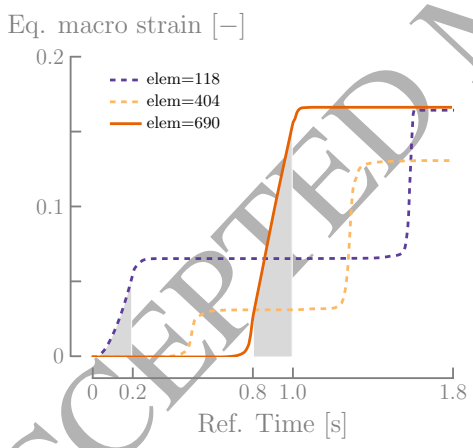

(c) Equivalent plastic strain.

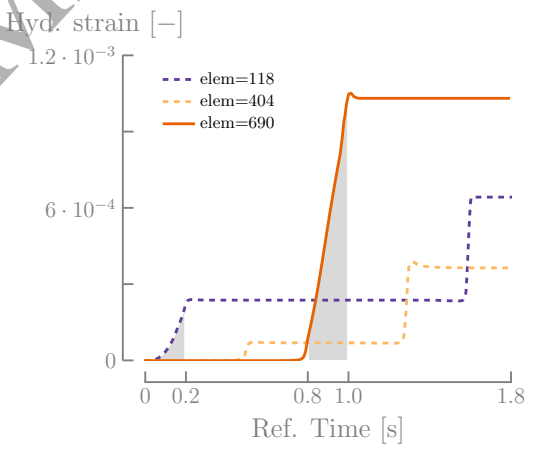

(d) Mean plastic strain.

Figure 4: State variables evolution in the line test for element numbers 118, 404 and 690. The shaded areas indicate the indent steps.

plain why element number 690 reaches a higher porosity than element number 118, as both elements show the same level of deformation (Fig. 4(c)). The reason of this higher value is based on the mean (volumetric) plastic strain evolution shown in Fig. 4(d). It is clear that element 690 attains a higher volumetric strain than element 118. Therefore, the porosity mechanism during the line test is mainly governed by the triaxiality and the volumetric parts of the plastic strain. As expected, the simulation does not predict material failure as no crack appeared within the experiment. Note that the coalescence stage is not activated within this line test, as the porosity is still far from the critical value f_{cr} =0.055 of the onset of coalescence.

4.2. Cone test

Fig. 5 shows the nominal geometry of a cone of wall angle α and 30 mm depth. The wall angle in this geometry is a measurement of the formability limits of SPIF for a determined material. For the DC01 steel of 1 mm thickness, 67° is the (experimental) maximum achievable wall angle without failure (Behera, 2013). SPIF cones with different wall angles are simulated and the porosity field is analyzed. The experimental measurements (forces and shapes) are not available for these cones, but the analytical formula of Aerens et al. (2009) is available to estimate the forming forces.

4.2.1. FE simulation

Fig. 5(c) depicts a 90° angle pie FE mesh consisting in 1492 `RESS` solid-shell elements, one element layer with 3 integration points through-thickness and 1344 `CFI3D` elements with 4 integration points. The toolpath is composed of 60 contours with a step down of 0.5 mm between two successive

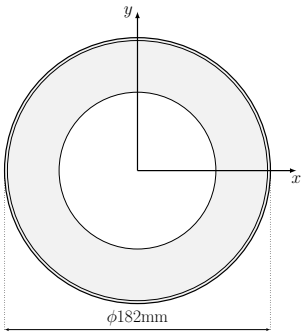

(a) Top view.

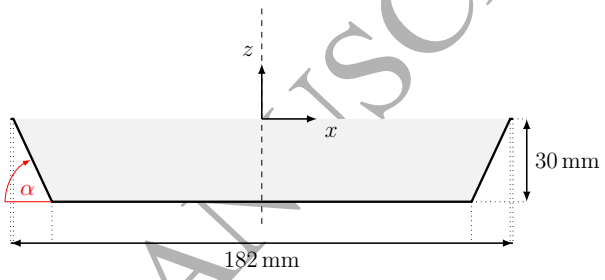

(b) Front view.

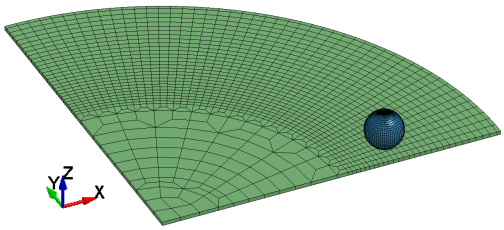

(c) FE mesh and tool tip.

Figure 5: Geometry and mesh of the cone test.

contours. As the experimental cone is clamped, the nodes along the outer circumferential part of the 90° pie mesh are completely fixed (in the three translations). In the other edges, rotational boundary conditions are imposed. For more details about the FE model, refer to Guzmán et al. (2012b) and Guzmán (2016).

Several FE simulations were carried out on SPIF cones with different wall angles using the set `shear` from Table 2. The FE predictions of the force are shown in Fig. 6 for four selected angles, two of them predicting material failure. The GTN model predicts a failure for a 48° cone. The model strongly

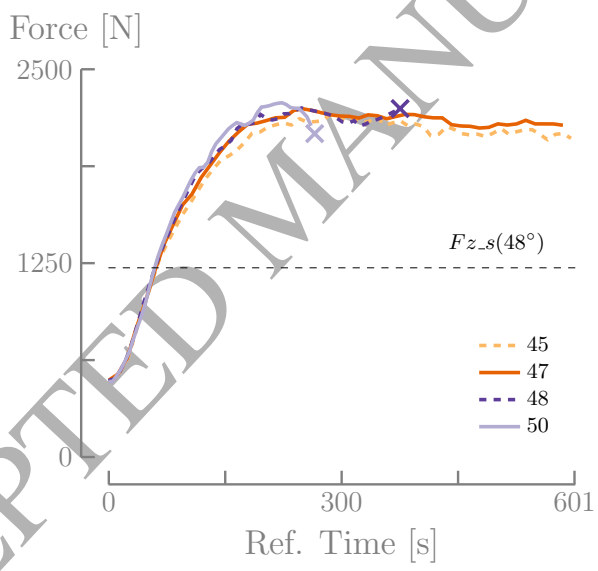

Figure 6: Axial force predictions for the cone test for different wall angles. The cross denotes the moment where $f = f_u$ in one FE. The analytical force Fz_s predicted by the Aerens et al. (2009) formula for a 48° wall angle is also depicted.

underestimates the failure angle, since for this material and thickness, the (experimental) critical wall angle is 67°. This issue is further analyzed in the

next section.

As experimental measurements are not available for this geometry, the predicted force by FE simulations is assessed using the formula proposed by Aerens et al. (2009). For a 48° cone the formula gives Fz_s =1222.49 N. Hence, the simulations overpredict the force in more than 100%. On the contrary, the force of the line test was well predicted compared to experimental results. The only difference in terms of the FE modeling between the line and the cone test is the introduction of the rotational boundary conditions. Nevertheless, the force evolution in the cone has different characteristics than those from the line test due to different toolpath strategies. The FE formulation can also play a role on the force prediction. Guzmán et al. (2012a) showed using the `SSH3D` solid-shell element for a line test simulation, that the element flexibility modified by EAS modes can severely decrease the force level. This was later confirmed by a pyramid test simulation by Duchêne et al. (2013). Potential reasons for high forces were studied by Sena et al. (2016) (boundary conditions, missing blankholder force modeling, friction coefficient, hardening modeling choice, element stiffness, etc.). In particular, for an AA7075-O aluminum alloy using the `RESS` element the hardening law has an important effect on the force level. The results using the Voce law, an isotropic hardening saturation law, are better than the Swift law but still overpredicts the force. In this case, the FE force prediction for an aluminum alloys is better compared to the prediction for the steel using the same `RESS` FE. The accuracy of the force prediction is a classical problem in SPIF, as demonstrated by the dispersion of the simulated results of the NUMISHEET benchmark (Elford et al., 2013).

4.2.2. Analysis of fracture prediction by the Gurson model

It is clear in Fig. 6 that the GTN model predicts fracture at an early stage. This wrong prediction of fracture can be attributed to different factors. Two hypothesis are presented hereafter.

First, the predicted force level which is 100% higher than the predicted value by the Aerens et al. (2009) formula. Nevertheless, a wrong force prediction does not necessarily mean a wrong damage prediction. If the reaction force predicted by the FE simulations would have been the reason why damage increases too quickly, then the 47° cone should have failed too. Therefore, the inaccurate force prediction of the FE is not the reason of the premature failure.

Second, an imprecise modeling of the deformation mechanisms, such as localization and thinning, can have a critical effect on the material formability. The shape and thickness distribution are correctly predicted by the `RESS` element, as shown in Fig. 2(a). This fact is also supported by previous simulations using the solid-shell element formulation (e.g. Duchêne et al., 2013; Sena et al., 2013). Localization is nonetheless a different aspect of the deformation. Malcher et al. (2012) showed that (in general) the GTN model does not accurately predicts the fracture strain, but it behaves relatively well under high and low triaxialities for the prediction of the force level and the displacement at fracture. Fig. 7 presents the equivalent plastic strain distribution for the 47° and 48° angle cones. The 47° is the limit case predicted by the model that does not fail. It is clear that strain does not localize and the plastic strain is evenly distributed, while for the 48° cone the strain localization is clear before failure. The maximum value of plastic

strain in Fig. 7(b) is around 0.8, which is below the usual values found on SPIF which are easily over 1.0 (e.g. Guzmán et al., 2012b). It is possible to observe a similar trend in the porosity distribution shown in Fig. 8. For the 48° cone, failure is preceded by localization of the equivalent plastic strain and porosity. The 47° cone does not fail because $f < f_F$ =0.135, so strain localization is triggered by the coalescence criterion of the GTN model. So, the coalescence criterion appears as a key point that can explain the inaccurate fracture prediction. This point is further discussed hereafter with the effect of shear-induced damage that the classic GTN extension does not take into account.

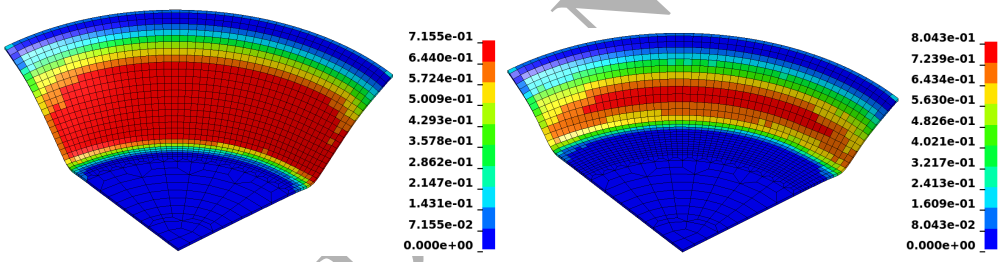

(a) 47° cone at the end of the simulation. (b) 48° cone at fracture.

Figure 7: Equivalent plastic strain distribution for the cone test simulation.

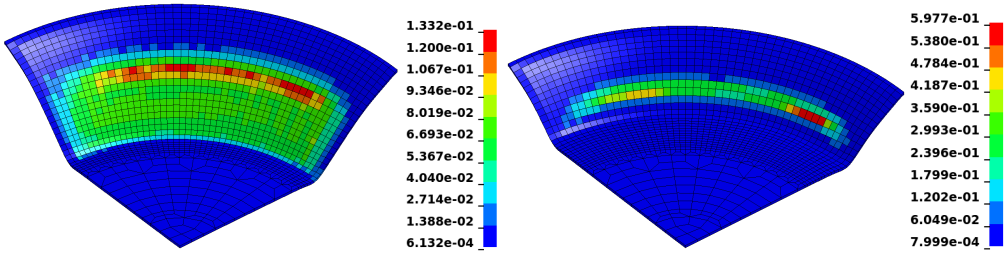

(a) 47° cone at the end of the simulation. (b) 48° cone at fracture.

Figure 8: Effective porosity distribution for the cone test simulation.

Four variants of GTN model and coalescence are analyzed in Table 3. Set `coa` is the classical coalescence model, without the shear extension. Set `shear` is the GTN model extended to shear. Set `coa+Thomason` and set `shear+Thomason` are the same as sets `coa` and `shear`, but including the Thomason criterion. Table 3 presents the maximum values on the whole FE mesh of the porosity reached when the coalescence starts (this value is only meaningful for the Thomason coalescence criterion) and the maximum effective porosity reached at the end of the process. It can be observed that:

Table 3: Numerical results for different types of coalescence models.

	`coa`	`coa+ Thomason`	`shear`	`shear+ Thomason`
Max. achievable wall angle	47°	51°	47°	51°
Max. porosity at initiation of coalescence	0.0055	0.0136	0.0055	0.0136
Max. effective porosity reached	0.1388	0.1644	0.2004	0.1546

1. The maximum achievable wall angles predicted by the variants of the GTN model are significantly smaller than the experimental value.
2. The shear extension has a very limited influence on the results.
3. The Thomason coalescence criterion permitted to increase the maximum achievable wall angle by delaying the onset of coalescence. Indeed, the porosity attained when the Thomason criterion is no longer fulfilled is way larger than the parameter f_{cr} of the classical GTN model.

4. The maximum effective porosity exceeded the failure limit f_F. However, such values only appear very locally in the simulations. These values were not considered to be associated with failure in this research.

Fig. 9 presents numerical results when the failure is predicted (i.e. when the maximum achievable wall angle is exceeded by 1°) for the `GTN+Shear+Thomason` variant. It appears that that the porosity reaches large values only in a zone around the final path of the tool. Locally, the porosity can be significantly larger than the failure limit. According to Fig. 9(b), coalescence appears in a similar zone.

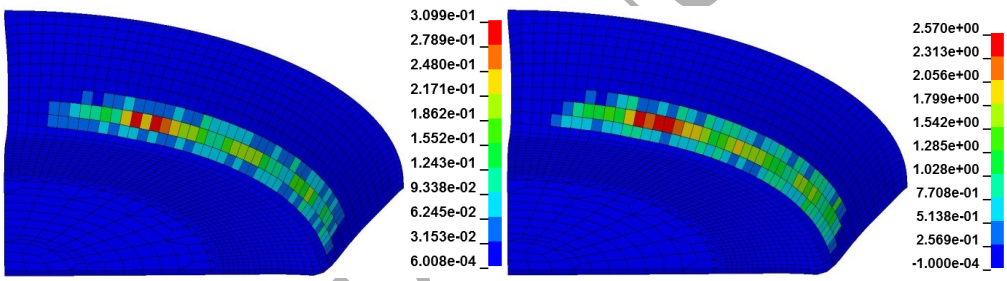

(a) Effective porosity.

(b) Difference between left hand side and right hand side of Thomason criterion (coalescence occurs when positive).

Figure 9: Numerical results for the `GTN+Shear+Thomason` model when failure is reached (the wall angle is 52°).

5. Gurson versus continuum approach

Summarizing, the most probable reason of the premature prediction of material failure by the GTN model is an inadequate coalescence criterion. Indeed, it has often been discussed that f_{cr} is not a sufficient criterion to

describe the initiation of fracture (e.g. Malcher et al., 2014). Triggering failure based only in the damage parameter (effective porosity) could be risky considering the complexity of the stress and strain path found on SPIF.

To further analyze the fracture prediction of the GTN model, a comparison will be given with other damage models. Ben Hmida (2014) used a Lemaitre type damage model in LS-Dyna explicit using a solid element. The identification of the elasto-plastic and damage parameters follows a two step procedure. Inverse analysis was used on a tensile test for elastoplastic parameters and then in a micro-SPIF test for the damage parameters. The simulations are able to predict the force level and failure in a micro-SPIF pyramid frustums. The Lemaitre model is based on the strain equivalence principle, which establishes a coupling between hardening and the damage variable. Malhotra et al. (2012) used a fracture model developed by Xue (2007). This model leads to good results when predicting the force and the depth at which fracture happens. In the Xue (2007) model, the damage evolution is function of the ratio of plastic strain and the fracture strain (the *self-similarity* hypothesis). In both cases, the main difference with the GTN model is that the damage models present a coupling between damage and the plastic strain. Originally, the Gurson (1977) model was developed to represent the deterioration of a porous material, based on unit-cells calculations. On the contrary, the Xue (2007) model is based on a theory where the plastic damage incorporates all the three stress invariants.

6. Conclusions and perspectives

In this paper, an evaluation of the GTN model extended to shear is performed. The effects of the Thomason coalescence criterion are also checked. A review of the state-of-the-art about formability and damage in SPIF is also presented. The line test is used to validate the simulations by comparing force and shape prediction with experimental results. In general, the results of the shape prediction are in good agreement with the experimental results. The fracture detection is correct for plane tests, while for SPIF the rupture associated to an angle of 67° is strongly underestimated. The good results obtained for the line tests are, unfortunately, not repeated on more complex shapes like the cone. For example, the force prediction is too high compared to experimental values, probably because of the boundary conditions. This is an issue that requires more research, as the deformation mechanisms are highly dependent on the process parameters so conclusions derived from some geometries are not necessarily repeatable in other shapes. On the other hand, the GTN model is capable to detect failure in a cone test, but the prediction is too premature compared to the experimental failure angle for the same material and geometry. After performing several FE simulations of SPIF cones with different wall angles, it is concluded that the GTN model underestimates the reference failure angle. The most probable reason for an imprecise failure modeling is the coalescence model, which depends only on the damage parameter (porosity). Moreover, the GTN model uncouples this damage parameter with hardening. Other models like the one proposed by Xue (2007) or the Lemaitre model used by Ben Hmida (2014), which predicts failure in the SPIF process, couple the damage evolution and

failure with the plastic strain. This research indicates that the developed failure mode cannot be predicted by the classical assumptions of the GTN model. Even if the damage model is capable to predict the loss of the loading capacity for notched specimens, the stress and strain path found on SPIF are different and certainly more complex.

Acknowledgment

C.F. Guzmán and E.I. Saavedra Flores acknowledge the support from the *Chilean National Commission for Scientific and Technological Research* (CONICYT), through Grant FONDECYT REGULAR No.1160691. S. Yuan, L. Duchêne and A.M. Habraken acknowledge the *Belgian Fund for Scientific Research* (FRS-FNRS) and the *Interuniversity Attraction Poles* (IAP) Program P7/21 (Belgian Science Policy) for its financial support. Computational resources have been provided by the *Consortium des Équipements de Calcul Intensif* (CÉCI), funded by the FRS-FNRS under Grant No. 2.5020.11.

References

Aerens, R., Eyckens, P., van Bael, A., Duflou, J. R., 2009. Force prediction for single point incremental forming deduced from experimental and FEM observations. Int. J. Adv. Manuf. Technol. 46 (9-12), 969–982.
URL http://www.springerlink.com/index/10.1007/s00170-009-2160-2

Allwood, J. M., Shouler, D. R., Tekkaya, A., 2007. The Increased Forming Limits of Incremental Sheet Forming Processes. In: Geiger, M., Duflou, J., Shirvani, B., Clarke, R., Di Lorenzo, R., Fratini, L. (Eds.), Key Eng. Mater. Vol. 344. Trans Tech Publications, Palermo, Italy, pp. 621–628.
URL http://www.scientific.net/KEM.344.621

Alves de Sousa, R. J., Cardoso, R. P., Fontes Valente, R. A., Yoon, J. W., Grácio, J. J., Natal Jorge, R. M., 2005. A new one-point quadrature enhanced assumed strain (EAS) solid-shell element with multiple integration points along thickness - Part I: geometrically linear applications. Int. J. Numer.

Methods Eng. 62 (7), 952–977.
URL http://doi.wiley.com/10.1002/nme.1226

Alves de Sousa, R. J., Cardoso, R. P., Fontes Valente, R. A., Yoon, J. W., Grácio, J. J., Natal Jorge, R. M., jul 2006. A new one-point quadrature enhanced assumed strain (EAS) solid-shell element with multiple integration points along thickness-part II: nonlinear applications. Int. J. Numer. Methods Eng. 67 (2), 160–188.
URL http://doi.wiley.com/10.1002/nme.1609

Armstrong, P., Frederick, C. O., 1966. A Mathematical Representation of the Multiaxial Bauschinger Effect. Technical report, Central Electricity Generating Board.

Bai, Y., Wierzbicki, T., 2008. A new model of metal plasticity and fracture with pressure and Lode dependence. Int. J. Plast. 24 (6), 1071–1096.
URL http://linkinghub.elsevier.com/retrieve/pii/S0749641907001246

Barsoum, I., Faleskog, J., 2007. Rupture mechanisms in combined tension and shear-Micromechanics. Int. J. Solids Struct. 44 (6), 5481–5498.
URL http://linkinghub.elsevier.com/retrieve/pii/S0020768306003921

Behera, A. K., 2013. Shape Feature Taxonomy Development for Toolpath Optimisation in Incremental Sheet Forming (Ontwikkeling van een taxonomie van vormkenmerken voor optimalisatie van gereedschapsbanen voor incrementeel omvormen). Phd thesis, Katholieke Universiteit Leuven.
URL https://lirias.kuleuven.be/handle/123456789/422489

Ben Bettaieb, A., Sena, J. I. V., Alves de Sousa, R. J., Valente, R., Habraken, A. M., Duchêne, L., 2015. On the comparison of two solid-shell formulations based on in-plane reduced and full integration schemes in linear and non-linear applications. Finite Elem. Anal. Des. 107, 44–59.
URL http://linkinghub.elsevier.com/retrieve/pii/S0168874X15001286

Ben Bettaieb, M., Lemoine, X., Duchêne, L., Habraken, A. M., 2011. On the numerical integration of an advanced Gurson model. Int. J. Numer. Methods Eng. 85 (8), 1049–1072.
URL http://doi.wiley.com/10.1002/nme.3010

Ben Hmida, R., 2014. Identification de lois de comportement de tôles en faibles épaisseurs par développement et utilisation du procédé de microformage incrémental. Ph.D. thesis, Franche-Comté électronique mécanique thermique et optique - Sciences et technologies.
URL http://www.theses.fr/2014BESA2042

Benzerga, A. A., Besson, J., 2001. Plastic potentials for anisotropic porous solids. Eur. J. Mech. - A/Solids 20 (3), 397–434.
URL http://linkinghub.elsevier.com/retrieve/pii/S0997753801011470

Bouffioux, C., Lequesne, C., Vanhove, H., Duflou, J. R., Pouteau, P., Duchêne, L., Habraken, A. M., 2011. Experimental and numerical study of an AlMgSc sheet formed by an incremental process. J. Mater. Process. Technol. 211 (11), 1684–1693.
URL http://linkinghub.elsevier.com/retrieve/pii/S0924013611001439

Brünig, M., 2003. An anisotropic ductile damage model based on irreversible thermodynamics. Int. J. Plast. 19 (10), 1679–1713.
URL http://linkinghub.elsevier.com/retrieve/pii/S0749641902001146

Brünig, M., Berger, S., Obrecht, H., 2000. Numerical simulation of the localization behavior of hydrostatic-stress-sensitive metals. Int. J. Mech. Sci. 42 (11), 2147–2166.
URL http://linkinghub.elsevier.com/retrieve/pii/S0020740300000023

Cescotto, S., Charlier, R., 1993. Frictional contact finite elements based on mixed variational principles. Int. J. Numer. Methods Eng. 36 (10), 1681–1701.
URL http://doi.wiley.com/10.1002/nme.1620361005

Cescotto, S., Grober, H., 1985. Calibration and application of an elastic viscoplastic constitutive equation for steels in hot-rolling conditions. Eng. Comput. 2 (2), 101–106.
URL http://www.emeraldinsight.com/10.1108/eb023607

Chaboche, J.-L., 1977. Viscoplastic constitutive equations for the description of cyclic and anisotropic behavior of metals. Bull. L'Academie Pol. des Sci. Série Sci. Tech. 25 (1), 33–42.

Chow, C., Wang, J., 1987. An anisotropic theory of continuum damage mechanics for ductile fracture. Eng. Fract. Mech. 27 (5), 547–558.
URL http://linkinghub.elsevier.com/retrieve/pii/0013794487901081

Chu, C. C., Needleman, A., 1980. Void Nucleation Effects in Biaxially Stretched Sheets. J. Eng. Mater. Technol. 102 (3), 249.
URL http://link.aip.org/link/JEMTA8/v102/i3/p249/s1{&}Agg=doi

Duchêne, L., Guzmán, C. F., Behera, A. K., Duflou, J. R., Habraken, A. M., 2013. Numerical Simulation of a Pyramid Steel Sheet Formed by Single Point Incremental Forming using Solid-Shell Finite Elements. In: Clarke, R., Leacock, A., Duflou, J. R., Merklein, M., Micari, F. (Eds.), Key Eng. Mater. Vol. 549. Trans Tech Publications, Belfast, United Kingdom, pp. 180–188.

Duflou, J. R., Verbert, J., Belkassem, B., Gu, J., Sol, H., Henrard, C., Habraken, A. M., 2008. Process window enhancement for single point incremental forming through multi-step toolpaths. CIRP Ann. - Manuf. Technol. 57 (1), 253–256.
URL http://linkinghub.elsevier.com/retrieve/pii/S0007850608000310

Elford, M., Saha, P., Seong, D., Haque, M. Z., Yoon, J. W., 2013. Benchmark 3 - Incremental sheet forming. In: Yoon, J. W., Stoughton, T. B., Rolfe, B., Beynon, J. H., Hodgson, P. (Eds.), AIP Conf. Proc. Vol. 227. American Institute of Physics, Melbourne, Australia, pp. 227–261.
URL http://link.aip.org/link/APCPCS/v1567/i1/p227/s1{&}Agg=doi

Emmens, W. C., 2011. Formability. Springer Berlin Heidelberg, Berlin.
URL http://link.springer.com/10.1007/978-3-642-21904-7

Emmens, W. C., a.H. van den Boogaard, 2007. Strain in Shear, and Material Behaviour in Incremental Forming. Key Eng. Mater. 344, 519–526.

Emmens, W. C., van den Boogaard, A., 2008. Tensile tests with bending: A mechanism for incremental forming. In: Boisse, P., Morestin, F., Vidal-Sallé, E. (Eds.), Int. J. Mater. Form. Vol. 1. Springer-Verlag, Lyon, France, pp. 1155–1158.

Emmens, W. C., van den Boogaard, A., 2010. Contact Effects in Bending Affecting Stress and Formability. Int. J. Mater. Form. 3 (S1), 1159–1162.

Emmens, W. C., van den Boogaard, A. H., 2009. An overview of stabilizing deformation mechanisms in incremental sheet forming. J. Mater. Process. Technol. 209 (8), 3688–3695.
URL http://dx.doi.org/10.1016/j.jmatprotec.2008.10.003http://linkinghub.elsevier.com/retrieve/pii/S0924013608007267

Eyckens, P., Belkassem, B., Henrard, C., Gu, J., Sol, H., Habraken, A. M., Duflou, J. R., Bael, A., van Houtte, P., 2010. Strain evolution in the single point incremental forming process: digital image correlation measurement and finite element prediction. Int. J. Mater. Form., 55–71.
URL http://www.springerlink.com/index/10.1007/s12289-010-0995-6

Eyckens, P., He, S., van Bael, A., van Houtte, P., Duflou, J. R., 2007. Forming Limit Predictions for the Serrated Strain Paths in Single Point Incremental Sheet Forming. In: AIP Conf. Proc. Vol. 908. AIP, Porto, Portugal, pp. 141–146.
URL http://link.aip.org/link/APCPCS/v908/i1/p141/s1{&}Agg=doi

Eyckens, P., van Bael, A., van Houtte, P., 2009. Marciniak-Kuczynski type modelling of the effect of Through-Thickness Shear on the forming limits of sheet metal. Int. J. Plast. 25 (12), 2249–2268.
URL http://linkinghub.elsevier.com/retrieve/pii/S0749641909000163

Filice, L., Fratini, L., Micari, F., 2002. Analysis of Material Formability in Incremental Forming. CIRP Ann. - Manuf. Technol. 51 (1), 199–202.
URL http://linkinghub.elsevier.com/retrieve/pii/S0007850607614991

Flores, P., Duchêne, L., Bouffioux, C., Lelotte, T., Henrard, C., Pernin, N., van Bael, A., He, S., Duflou, J. R., Habraken, A. M., 2007. Model identification and FE simulations: Effect of different yield loci and hardening laws in sheet forming. Int. J. Plast. 23 (3), 420–449.
URL http://linkinghub.elsevier.com/retrieve/pii/S0749641906001136

Frederick, C. O., Armstrong, P., 2007. A mathematical representation of the multiaxial Bauschinger effect. Mater. High Temp. 24 (1), 1–26.

Gao, X., Zhang, G., Roe, C., 2009. A Study on the Effect of the Stress State on Ductile Fracture. Int. J. Damage Mech. 19 (1), 75–94.
URL http://ijd.sagepub.com/cgi/doi/10.1177/1056789509101917

Garrison, W., Moody, N., 1987. Ductile fracture. J. Phys. Chem. Solids 48 (11), 1035–1074.
URL http://linkinghub.elsevier.com/retrieve/pii/0022369787901181

Gologanu, M., Leblond, J.-B., Perrin, G., Devaux, J., 1996. Recent extensions of Gurson's model for porous ductile materials. In: Int. Semin. Micromechanics. Udine, Italy, pp. 61–130.

Gurson, A. L., 1977. Continuum theory of ductile rupture by void nucleation and growth: Part I-Yield criteria and flow rules for porous ductile media. J. Eng. Mater. Technol. 99 (1), 2–15.

Guzmán, C. F., 2016. Experimental and Numerical Characterization of Damage and Application to Incremental Forming. Phd thesis, Université de Liège.
URL http://hdl.handle.net/2268/192884

Guzmán, C. F., Ben Bettaieb, A., Sena, J. I. V., Alves de Sousa, R. J., Habraken, A. M., Duchêne, L., 2012a. Evaluation of the Enhanced Assumed Strain and Assumed Natural Strain in the SSH3D and RESS3 Solid Shell Elements for Single Point Incremental Forming Simulation. In: Merklein, M., Hagenah, H. (Eds.), Key Eng. Mater. Vol. 504-506. Erlangen, Germany, pp. 913–918.
URL http://www.scientific.net/KEM.504-506.913

Guzmán, C. F., Gu, J., Duflou, J. R., Vanhove, H., Flores, P., Habraken, A. M., 2012b. Study of the geometrical inaccuracy on a SPIF two-slope pyramid by finite element simulations. Int. J. Solids Struct. 49 (25), 3594–3604.
URL http://linkinghub.elsevier.com/retrieve/pii/S0020768312003010

Guzmán, C. F., Saavedra Flores, E. I., 2016. Numerical integration of anisotropic yield criterion for porous solids. In: Cuad. Mecánica Comput. Vol. 14. Arica, Chile, pp. 151–158.

Habraken, A. M., Cescotto, S., 1998. Contact between deformable solids: The fully coupled approach. Math. Comput. Model. 28 (4-8), 153–169.
URL http://linkinghub.elsevier.com/retrieve/pii/S0895717798001150

Ham, M., Jeswiet, J., 2007. Forming limit curves in single point incremental forming. CIRP Ann. - Manuf. Technol. 56, 277–280.

Hill, R., may 1948. A Theory of the Yielding and Plastic Flow of Anisotropic Metals. Proc. R. Soc. A Math. Phys. Eng. Sci. 193 (1033), 281–297.
URL http://rspa.royalsocietypublishing.org/cgi/doi/10.1098/rspa.1948.0045http://rspa.royalsocietypublishing.org/content/193/1033/281.abstract

Hirt, G., Ames, J., Bambach, M., Kopp, R., 2004. Forming strategies and process modelling for CNC incremental sheet forming. CIRP Ann. - Manuf. Technol. 53 (1), 203–206.
URL http://www.sciencedirect.com/science/article/pii/S0007850607606799

Jeswiet, J., Micari, F., Hirt, G., Bramley, A., Duflou, J. R., Allwood, J. M., 2005. Asymmetric Single Point Incremental Forming of Sheet Metal. CIRP Ann. - Manuf. Technol. 54 (2), 88–114.
URL http://linkinghub.elsevier.com/retrieve/pii/S0007850607600213http://www.sciencedirect.com/science/article/B8CXH-4SRVXM5-5/2/260e56998a9f7ed28f6f8ed20bf363cc

Jeswiet, J., Young, D., 2005. Forming limit diagrams for single-point incremental forming of aluminium sheet. Proc. Inst. Mech. Eng. Part B J. Eng. Manuf. 219 (4), 359–364.
URL http://pib.sagepub.com/lookup/doi/10.1243/095440505X32210

Keeler, S. P., Backofen, W. A., 1963. Plastic instability and fracture in sheets stretched over rigid punches. Trans. Am. Soc. Met. 56, 25–28.

Lemaitre, J., 1985. A Continuous Damage Mechanics Model for Ductile Fracture. J. Eng. Mater. Technol. 107 (1), 83.
URL http://link.aip.org/link/JEMTA8/v107/i1/p83/s1{&}Agg=doi

Li, K., Cescotto, S., 1997. An 8-node brick element with mixed formulation for large deformation analyses. Comput. Methods Appl. Mech. Eng. 141 (1-2), 157–204.
URL http://linkinghub.elsevier.com/retrieve/pii/S0045782596010717

Lievers, W., Pilkey, A., Lloyd, D., 2004. Using incremental forming to calibrate a void nucleation model for automotive aluminum sheet alloys. Acta Mater. 52 (10), 3001–3007.

Malcher, L., Andrade Pires, F. M., César de Sá, J., 2012. An assessment of isotropic constitutive models for ductile fracture under high and low stress triaxiality. Int. J. Plast. 30-31, 81–115.
URL http://linkinghub.elsevier.com/retrieve/pii/S0749641911001690

Malcher, L., Andrade Pires, F. M., César de Sá, J., 2014. An extended GTN model for ductile fracture under high and low stress triaxiality. Int. J. Plast. 54, 193–228.
URL http://linkinghub.elsevier.com/retrieve/pii/S0749641913001708

841 Malhotra, R., Xue, L., Belytschko, T., Cao, J., 2012. Mechanics of fracture in single point incremental
842 forming. J. Mater. Process. Technol. 212 (7), 1573–1590.
843 URL http://linkinghub.elsevier.com/retrieve/pii/S0924013612000726

844 Marciniak, Z., Kuczynski, K., 1967. Limit strains in the processes of stretch-forming sheet metal. Int. J.
845 Mech. Sci. 9 (9), 609–620.
846 URL http://linkinghub.elsevier.com/retrieve/pii/0020740367900665

847 Mühlich, U., Brocks, W., 2003. On the numerical integration of a class of pressure-dependent plasticity
848 models including kinematic hardening. Comput. Mech. 31 (6), 479–488.
849 URL http://link.springer.com/10.1007/s00466-003-0454-z

850 Nahshon, K., Hutchinson, J. W., 2008. Modification of the Gurson Model for shear failure. Eur. J. Mech.
851 - A/Solids 27 (1), 1–17.
852 URL http://linkinghub.elsevier.com/retrieve/pii/S0997753807000721

853 Nielsen, K. L., Tvergaard, V., 2009. Effect of a shear modified Gurson model on damage development in
854 a FSW tensile specimen. Int. J. Solids Struct. 46 (3-4), 587–601.
855 URL http://linkinghub.elsevier.com/retrieve/pii/S0020768308003752

856 Nielsen, K. L., Tvergaard, V., 2010. Ductile shear failure or plug failure of spot welds modelled by modified
857 Gurson model. Eng. Fract. Mech. 77 (7), 1031–1047.
858 URL http://linkinghub.elsevier.com/retrieve/pii/S0013794410001128

859 Reddy, N. V., Lingam, R., Cao, J., 2015. Incremental Metal Forming Processes in Manufacturing. In: Nee,
860 A. Y. C. (Ed.), Handb. Manuf. Eng. Technol. Springer London, London, Ch. 9, pp. 411–452.
861 URL http://link.springer.com/10.1007/978-1-4471-4670-4

862 Sena, J. I. V., Guzmán, C. F., Duchêne, L., Habraken, A. M., Valente, R. A. F., Alves de Sousa, R. J.,
863 2013. Numerical simulation of a conical shape made by single point incremental. In: Yoon, J. W.,
864 Stoughton, T. B., Rolfe, B., Beynon, J. H., Hodgson, P. (Eds.), AIP Conf. Proc. American Institute
865 of Physics, Melbourne, Australia, pp. 852–855.
866 URL http://scitation.aip.org/content/aip/proceeding/aipcp/10.1063/1.4850104http://link.
867 aip.org/link/APCPCS/v1567/i1/p852/s1{&}Agg=doi

868 Sena, J. I. V., Lequesne, C., Duchene, L., Habraken, A.-M., Valente, R. A., Alves de Sousa, R. J.,
869 2016. Single point incremental forming simulation with adaptive remeshing technique using solid-shell
870 elements. Eng. Comput. 33 (5), 1388–1421.
871 URL http://www.emeraldinsight.com/doi/10.1108/EC-06-2015-0172

872 Seong, D., Haque, M. Z., Kim, J. B., Stoughton, T. B., Yoon, J. W., 2014. Suppression of necking in
873 incremental sheet forming. Int. J. Solids Struct. 51 (15-16), 2840–2849.
874 URL http://dx.doi.org/10.1016/j.ijsolstr.2014.04.007

875 Silva, M. B., Nielsen, P. S., Bay, N., Martins, P., 2011. Failure mechanisms in single-point incremental
876 forming of metals. Int. J. Adv. Manuf. Technol. 56 (9-12), 893–903.
877 URL http://www.springerlink.com/index/10.1007/s00170-011-3254-1

878 Silva, M. B., Skjoedt, M., Martins, P., Bay, N., 2008. Revisiting the fundamentals of single point incre-
879 mental forming by means of membrane analysis. Int. J. Mach. Tools Manuf. 48 (1), 73–83.
880 URL http://linkinghub.elsevier.com/retrieve/pii/S0890695507001289

881 Simo, J. C., Rifai, M. S., jun 1990. A class of mixed assumed strain methods and the method of incom-
882 patible modes. Int. J. Numer. Methods Eng. 29 (8), 1595–1638.
883 URL http://doi.wiley.com/10.1002/nme.1620290802

884 Stoughton, T. B., Yoon, J. W., 2011. A new approach for failure criterion for sheet metals. Int. J. Plast.
885 27 (3), 440–459.
886 URL http://linkinghub.elsevier.com/retrieve/pii/S0749641910000951

887 Thomason, P., 1990. Ductile fracture of metals. Pergamon Press.

888 Tvergaard, V., 1981. Influence of voids on shear band instabilities under plane strain conditions. Int. J.
889 Fract. 17 (4), 389–407.
890 URL http://www.springerlink.com/index/10.1007/BF00036191

891 Tvergaard, V., Needleman, A., 1984. Analysis of the cup-cone fracture in a round tensile bar. Acta Metall.
892 32 (1), 157–169.
893 URL http://linkinghub.elsevier.com/retrieve/pii/000161608490213X

894 Voyiadjis, G. Z., Kattan, P. I., 1992. A plasticity-damage theory for large deformation of solids-I. Theo-
895 retical formulation. Int. J. Eng. Sci. 30 (9), 1089–1108.
896 URL http://linkinghub.elsevier.com/retrieve/pii/002072259290059P

897 Xue, L., 2007. Damage accumulation and fracture initiation in uncracked ductile solids subject to triaxial
898 loading. Int. J. Solids Struct. 44 (16), 5163–5181.
899 URL http://linkinghub.elsevier.com/retrieve/pii/S002076830600552X

900 Xue, L., Belytschko, T., 2010. Fast methods for determining instabilities of elastic-plastic damage models
901 through closed-form expressions. Int. J. Numer. Methods Eng. 84 (12), 1490–1518.

902 Zhang, K., Bai, J., François, D., 2001. Numerical analysis of the influence of the Lode parameter on void
903 growth. Int. J. Solids Struct. 38 (32-33), 5847–5856.
904 URL http://www.sciencedirect.com/science/article/pii/S0020768300003917http://linkinghub.
905 elsevier.com/retrieve/pii/S0020768300003917

906 Zhang, Z., Thaulow, C., Ødegård, J., 2000. A complete Gurson model approach for ductile fracture. Eng.
907 Fract. Mech. 67 (2), 155–168.
908 URL http://linkinghub.elsevier.com/retrieve/pii/S0013794400000552